

Piezoionic Elastomers by Phase and Interface Engineering for High-Performance Energy-Harvesting Ionotronics

Weiyan Zhu, Baohu Wu, Zhouyue Lei,* and Peiyi Wu*

Piezoionic materials play a pivotal role in energy-harvesting ionotronics. However, a persistent challenge lies in balancing the structural requirements for voltage generation, current conduction, and mechanical adaptability. The conventional approach of employing crystalline heterostructures for stress concentration and localized charge separation, while effective for voltage generation, often compromises the stretchability and long-range charge transport found in homogeneous quasisolid states. Herein, phase and interface engineering strategy is introduced to address this dilemma and a piezoionic elastomer is presented that seamlessly integrates ionic liquids and ionic plastic crystals, forming a finely tuned microphase-separated structure with an intermediate phase. This approach promotes charge separation via stress concentration among hard phases while leveraging the high ionic charge mobility in soft and intermediate phases. Impressively, the elastomer achieves an extraordinary piezoionic coefficient of about 6.0 mV kPa⁻¹, a more than threefold improvement over current hydrogels and ionogels. The resulting power density of 1.3 μW cm⁻³ sets a new benchmark, exceeding that of state-of-the-art piezoionic gels. Notably, this elastomer combines outstanding stretchability, remarkable toughness, and rapid self-healing capability, underscoring its potential for real-world applications. This work may represent a stride toward mechanically robust energy harvesting systems and provide insights into ionotronic systems for human-machine interaction.

1. Introduction

Piezoionic and piezoelectric materials play a pivotal role in converting mechanical energy into electricity, crucial for energy harvesting and human–machine interaction in ionotronic systems. [1–4] Traditional piezoelectric materials, including

W. Zhu, Z. Lei, P. Wu

State Key Laboratory for Modification of Chemical Fibers and Polymer

College of Chemistry and Chemical Engineering Center for Advanced Low-Dimension Materials

Donghua University
Shanghai 201620, China

E-mail: leizhouyue@dhu.edu.cn; wupeiyi@dhu.edu.cn

B. Wu

Jülich Centre for Neutron Science (JCNS) at Heinz Maier-Leibnitz Zentrum (MLZ) Forschungszentrum Jülich

Lichtenbergstr. 1, 85748 Garching, Germany

inorganic, organic, and hybrid varieties, derive the piezoelectric effect from uneven charge distribution induced by stress concentration in crystalline lattices. [5–7] However, the brittleness of the heterogeneous crystal structures results in a trade-off between optimal electrical performance and mechanical properties. [3,8] Despite advances such as layer-by-layer self-assembly, achieving enhanced stretchability and self-healing remains challenging, hindering seamless integration into stretchable ionotronic systems that interface with biological systems. [8]

On the other hand, the piezoionic effect relies on different cationic and anionic mobilities under pressure, providing an alternative for harnessing mechanical energy. Unlike conventional piezoelectric materials, which mainly confine electron charges within crystals, ionically conductive materials such as hydrogels or ionogels boast significantly higher concentrations of free charge carriers (mobile ions) dispersed in homogeneous quasisolid structures. [9–12] This enables the generation of substantial iondriven currents for external circuits. [1.2] In addition, piezoionic materials often

incorporate soft, stretchable polymer networks as matrices, effectively addressing challenges faced by conventional piezoelectric materials in adapting to biological tissues. [13–16] However, the homogeneous or nanophase-separated quasisolid structures dissipate rather than concentrate stress, making it difficult to induce localized charge separation. Consequently, this leads to a comparatively reduced voltage response under pressure, limiting voltage increments and reducing energy conversion efficiency during deformation. Moreover, hydrogel-based piezoionic materials face environmental instability when integrated into stretchable ionotronic systems, requiring complex encapsulation methods. [17–19] Therefore, there is a critical need to develop piezoionic materials that take advantage of both mechanical adaptability and high ionic conductivity, while overcoming the limitations of conventional piezoionic hydrogels and ionogels.

Herein, we present an approach by incorporating an intermediate phase into microphase-separated ionic elastomers through phase and interface engineering. This strategy leverages microphase separation to enhance localized stress concentration, thereby improving the response voltages. Meanwhile, the

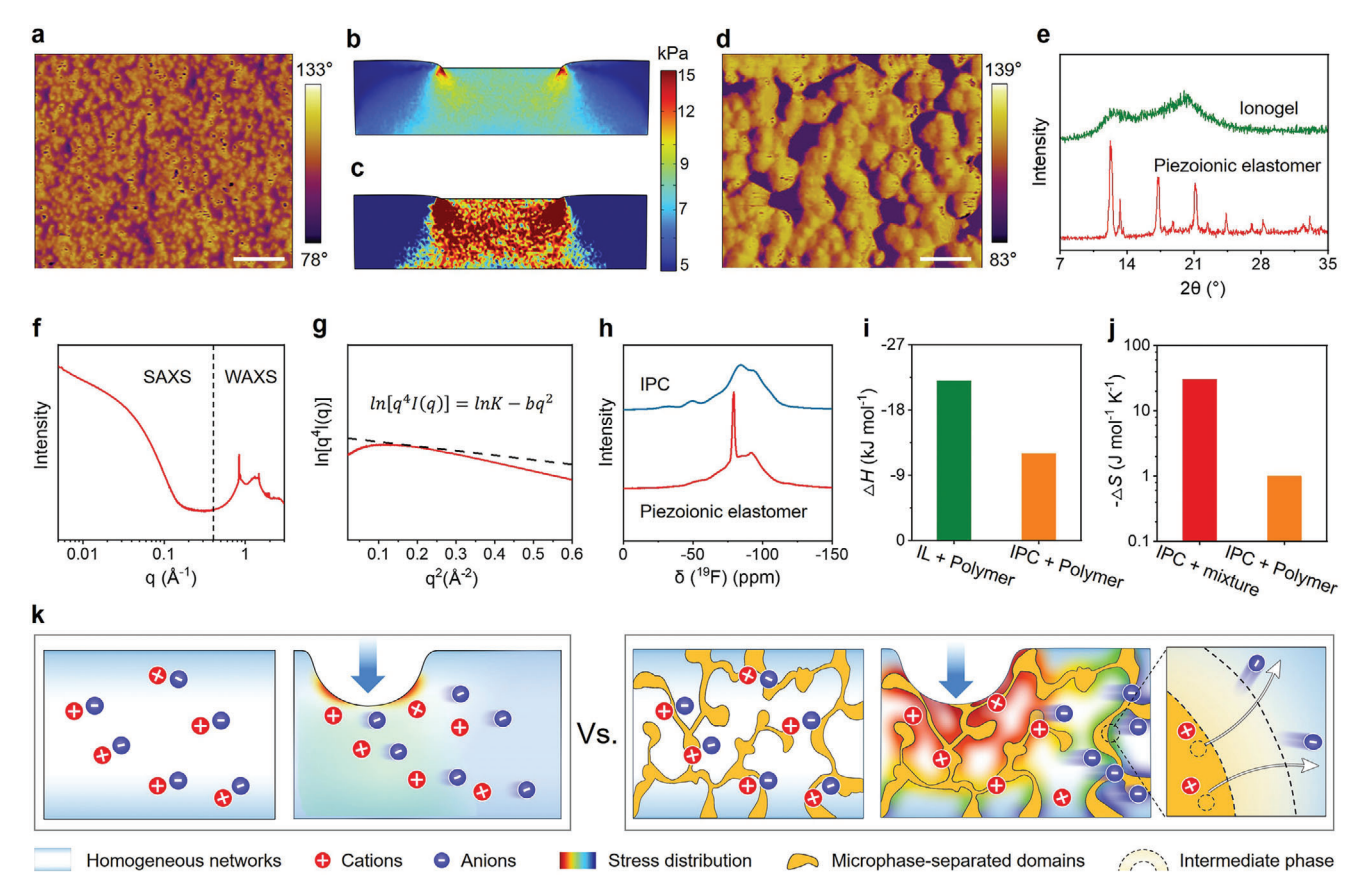


Figure 1. a) An AFM phase image of PVDF-HFP/EMIM TFSI ionogel. Scale bar: 4 μm. b) Finite element simulation of stress distribution in homogeneous or nanoscale phase-separated structures under mechanical loading. c) Finite element simulation of stress distribution when the phase separation size increases to the micrometer scale. d) An AFM phase image of the piezoionic elastomer. Scale bar: 4 μm. e) XRD profiles of the PVDF-HFP/IL ionogel and the piezoionic elastomer. f) The WAXS–SAXS curve of the piezoionic elastomer. g) The Porod plot of the piezoionic elastomer. The dashed line indicates a negative deviation from Porod's law. h) Static ¹⁹F NMR spectra of IPC and the piezoionic elastomer. i) The ΔH when the PVDF-HFP (polymer) is titrated with IL (IL + Polymer) and the polymer is titrated with IPC (IPC + Polymer). j) The ΔS when the PVDF-HFP (polymer) is titrated with IPC (IPC + Polymer) and the polymer–IL mixture is titrated with IPC (IPC + mixture). k) Schematic illustration of the differential ionic displacement, charge imbalance, and electric field generated in the homogeneous ionogel and the piezoionic elastomer under mechanical loading. The rainbow colors indicate stress distribution in the homogeneous ionogel and the piezoionic elastomer.

intermediate phase design preserves compatibility between different phases and facilitates pressure-driven ion convection, which is critical for generating large currents. Furthermore, the piezoionic elastomer demonstrates remarkable stretchability, toughness, and self-healing capability. Its potential extends beyond heightened energy conversion efficiency, as it can also serve as sensitive sensors and logic processing units in stretchable ionotronic systems for seamless human–machine interaction.

2. Results

2.1. Phase and Interface Engineering in Piezoionic Elastomers

Many soft piezoionic materials reported to date, such as hydrogels and ionogels, often exhibit homogeneous or nanoscale phase-separated structures. Taking an ionogel as an example (i.e., an ionic liquid (IL) 1-ethyl-3-methylimidazolium bis(trifluoromethylsulfonyl)imide (EMIM TFSI) dispersed in polyvinylidene fluoride-hexafluoropropylene (PVDF-HFP) en-

tangled polymer networks), its phase separation size is \approx 350 nm (less than 1 µm, Figure 1a). Finite element simulations using COMSOL reveal that, the ionogel undergoes stress dissipation rather than concentration during mechanical loading (Figure 1b and Note S1 (Supporting Information)). This impedes charge separation under pressure, resulting in a small voltage response (Figure S1, Supporting Information). By contrast, when the phase separation size increases to the micrometer scale, the material demonstrates notable stress concentration under mechanical loading (Figure 1c and Note S1 (Supporting Information)). Therefore, it is imperative to internally introduce microphaseseparated heterogeneous structures in soft materials to enhance localized charge separation. Additionally, the incorporation of an intermediate phase within these heterogeneous structures is crucial to ensure long-range charge transport, preventing macroscopic phase separation while maintaining mechanical softness and stretchability.

To tailor the phase and interface characteristics of piezoionic elastomers, this study proposes a method for the simultaneous incorporation of an IL and an ionic plastic crystal (IPC)

into an elastic matrix, following three key design principles: i) microphase-separated structure: establishes a microphase-separated structure by leveraging the poor compatibility between the IPC and the polymer networks; ii) intermediate phase engineering: designs the IL and IPC with the shared anion, ensuring compatibility between the IL and the IPC and thus engineers an intermediate phase that bridges the heterogeneous microphases; iii) enhanced cation—anion mobility disparity: highlights the difference in the mobility of cations and anions under pressure by tethering cations to the polymer network through cation—dipole interactions. This approach facilitates the release of more free anions.

To validate the feasibility of the design principles, we introduce an IPC (C2mpyr TFSI, N-ethyl-N-methylpyrrolidinium bis(tirfluoromethylsulfonylimide) into the PVDF-HFP/EMIM TFSI ionogel (Figure S2, Supporting Information). Atomic force microscope (AFM) analysis reveals a microphase-separated structure within the elastomer matrix, which increases to ≈2 µm with the addition of 55 wt% IPC (Figure 1d). In contrast to the amorphous structure of the ionogel, the X-ray diffraction (XRD) pattern of the piezoionic elastomer clearly shows crystalline peaks (12.3°, 13.2°, 17.2°, and 21.7°), confirming the incorporation of the heterogeneous crystalline phase of IPC (Figure 1e and Figure S3 (Supporting Information)). Additionally, the half-width of the crystalline diffraction bands widens with the addition of IL, indicating the formation of an intermediate amorphous phase at the interface between IPC and the polymer matrix.[20,21] Synchrotron wide and small angle X-ray scattering (WAXS-SAXS) also shows prominent crystalline peaks in the high q region, confirming the presence of a crystalline phase structure in the elastomer (Figure 1f). [22] Furthermore, the $\ln(I(q)q^4) \sim q^2$ pattern of the piezoionic elastomer exhibits a negative slope in the high q region, indicating a negative deviation from Porod's law (Figure 1g and Note S2 (Supporting Information)),[23] which is consistent with the XRD results. Both suggest the existence of an interfacial layer between the soft and hard phases in the piezoionic elastomer, which favors the enhancement of compatibility between different phases.

Single-pulse static nuclear magnetic resonance (19F NMR) spectroscopy further illuminates ion dynamics at the intermediate phase interface. Unlike the broad line shape observed in ion plastic crystals, the static ¹⁹F NMR of the piezoionic elastomer reveals two peaks within the range of -100 to -50 ppm (Figure 1h). Specifically, a narrow peak at -79 ppm is superimposed on a broader band at -92.3 ppm and indicates the presence of highly mobile [TFSI]⁻ anions in the piezoionic elastomer,^[20,21] driving ion convection under pressure. Isothermal titration calorimetry offers further insights into the intermolecular interactions from a thermodynamic perspective.^[24] When PVDF-HFP (polymer) is titrated with IL, a strong cation-dipole interaction forms between IL and PVDF-HFP, resulting in a large exothermic enthalpy (ΔH $= -21.8 \text{ kJ} \text{ mol}^{-1}$) (Figure 1i and Figure S4 and Note S3 (Supporting Information)). By contrast, when the polymer is titrated with IPC, a ΔH of only -12.0 kJ mol⁻¹ is observed, indicating that the cation-dipole interaction between IPC and the polymer is weaker than that between IL and the polymer. This observation is consistent with the small entropy change $(-1.0 \text{ J mol}^{-1} \text{ K}^{-1})$ when the polymer is titrated with IPC, confirming the limited compatibility between IPC and the polymer. Notably, when the polymerIL mixture is titrated with IPC, the entropy change increases to $-30.4 \,\mathrm{J}\,\mathrm{mol}^{-1}\,\mathrm{K}^{-1}$ (Figure 1j). This is further confirmed through macroscopic observations. In contrast to the evident precipitation observed in the mixture of IPC and PVDF-HFP, IPC shows uniform dispersion in the acetone solution of IL and PVDF-HFP (Figure S5, Supporting Information). Besides, compared to the elastomers where IL and IPC share the same anion, when IL and IPC have different anions, the polymer/IL/IPC composites exhibit poor mechanical performance (Figure S6, Supporting Information). Therefore, when IPC and IL share the same anion, it promotes good compatibility and the formation of an intermediate phase that bridges heterogeneous microphases, thereby establishing pathways for efficient ion convection.

Given that the piezoionic effect arises from the uneven ion distribution when a pressure gradient is applied, our design utilizes microphase separation to amplify the local stress concentration, thereby enhancing the piezoionic transduction (Figure 1k). Moreover, the intermediate phase design ensures compatibility between different phases, facilitating ion convection under pressure, resulting in a large ion current. This innovative strategy is poised to generate a significant gradient in ion distribution, ultimately boosting the piezoionic effect.

2.2. Enhanced Piezoionic Performance

In the case of the PVDF-HFP/EMIM TFSI ionogel, its nanophase-separated structure results in a voltage response of only 10 mV under a 15 kPa pressure, which is comparable to piezoionic hydrogels. Previous COMSOL analyses have shown that the uniform elastic network leads to stress dissipation, hindering ion charge separation and resulting in a low response voltage. In the absence of IL, the PVDF-HFP/IPC demonstrates a high voltage response of ≈140 mV under a 15 kPa pressure (Figure \$7, Supporting Information). However, it undergoes macroscopic phase separation, making it brittle and rigid (Figure S8, Supporting Information). It displays a weak current of <1 nA under 15 kPa pressure. This is because the hard phase impedes the movement and convection of mobile ions within the heterogeneous structure upon stress-induced local charge separation. To address this issue, the mass fraction of IPC was optimized. With increasing IPC content, the piezoionic elastomer exhibits an increase in piezoionic voltage (Figures S9 and S10, Supporting Information), likely attributed to the generation of a microphase-separated structure. However, as the IPC content continues to increase, the piezoionic current and ionic conductivity gradually decrease (Figures S11 and S12, Supporting Information). At an IPC mass concentration of 55 wt%, the elastomer demonstrates both high piezoionic voltage and current, reaching the maximum theoretical output power ($P_{\text{out}} = \frac{UI}{4}$) (Figure \$13, Supporting Information). It is stretchable and exhibits an ionic conductivity of about 0.3 S m⁻¹ (Figure S14, Supporting Information), surpassing that of many traditional ionic elastomers $(0.003-0.2 \text{ S m}^{-1}).^{[25-27]}$ Upon applying a pressure of 15 kPa to the piezoionic elastomer with a thickness of 0.3 mm, it generates an open-circuit voltage of up to 90 mV and a short-circuit current of 92 nA (Figure 2a). Even after repeated step compressions, the deviations in generated voltage and current are less than 4%, demonstrating the excellent stability of the piezoionic

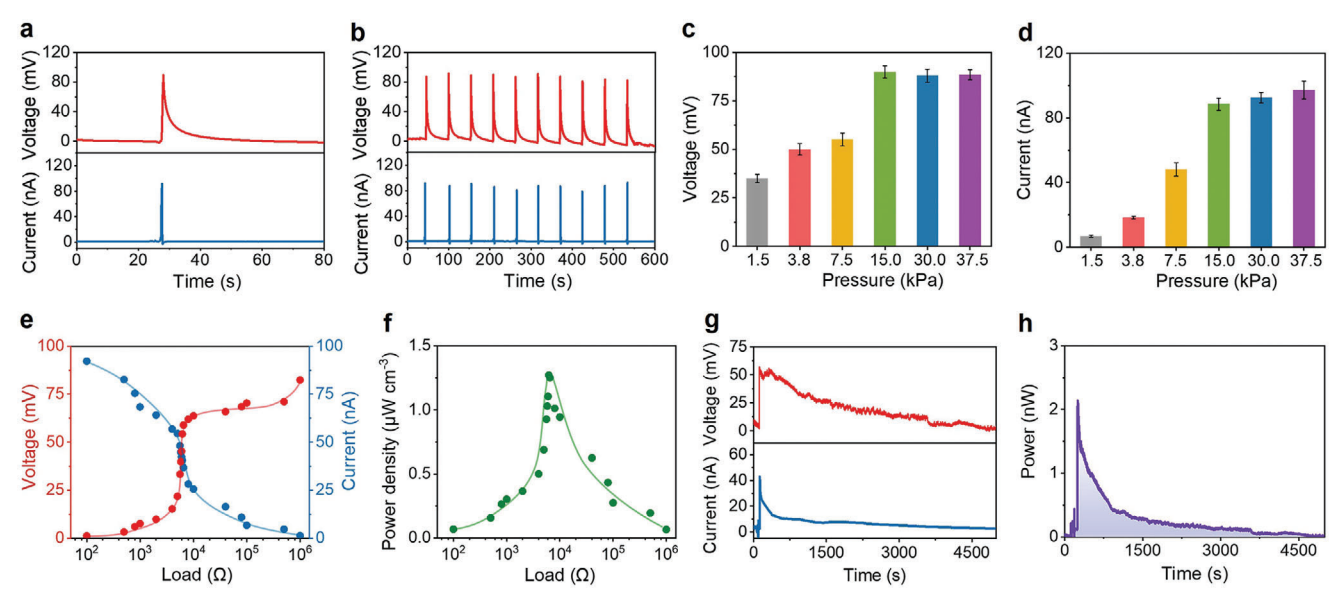


Figure 2. a) Voltage and current responses of the piezoionic elastomer at a pressure of 15 kPa. b) Voltage and current responses under repeated step compressions at a pressure of 15 kPa. c) Voltage responses of the piezoionic elastomer at different pressures. d) Current responses of the piezoionic elastomer at different pressures. e) Voltage and current versus R_{load} plots of the piezoionic elastomer at a pressure of 15 kPa. f) The P_{out} versus R_{load} plots of the piezoionic elastomer at a pressure of 15 kPa. g) Voltage and current curves of the discharge process at a constant pressure of 15 kPa. The thickness of the piezoionic elastomer is 1 mm, and R_{load} is 10 200 Ω. h) The P_{out} curve of the discharge process at a constant pressure of 15 kPa. The thickness of the piezoionic elastomer is 1 mm and R_{load} is 10 200 Ω.

performance (Figure 2b). The simultaneous generation of high voltage and large current is attributed to stress concentration facilitating charge separation, coupled with the presence of an intermediate phase alongside a continuous phase that aids ion transport and convection. Notably, when IL and IPC have different anions, the polymer/IL/IPC composites exhibit low piezoionic voltage (3–29 mV), low current (5–17 nA), and poor mechanical performance (Figures S6–S15, Supporting Information). The decline is attributed to the poor compatibility between IPC and IL with different anions. This observation underscores the effectiveness of employing the same anion to create an intermediate phase that bridges the heterogeneous microphases.

Different pressures result in different voltages and currents. Under low pressure (<15 kPa), increasing pressure leads to a gradual rise in voltage. Once the pressure exceeds 15 kPa, the open-circuit voltage is almost unchanged (Figure 2c and Figure S16 (Supporting Information)). According to the formula $\nabla V =$ $a\nabla P$, where a represents the piezoionic coefficient and ∇P signifies pressure gradient, the maximum piezoionic coefficient of the elastomer reaches about 6.0 mV kPa-1 (Figure S17, Supporting Information). This is much higher than that of existing piezoionic ionogels (about 0.1 mV kPa⁻¹),^[6] an improvement of nearly 60 times. It also exceeds the piezoionic coefficient of the state-of-the-art hydrogel (1.78 mV kPa⁻¹) by nearly 3 times.^[11] Additionally, the current generated by the piezoionic elastomers is nearly two orders of magnitude higher than that of traditional piezoelectric materials which are about several nanoamperes.^[28] The trend in response current closely mirrors that of the response voltage. Below 15 kPa pressure, the short-circuit current increases proportionally. Yet, beyond 15 kPa pressure, the current increment diminishes, aligning with levels observed in existing

piezoionic hydrogels (Figure 2d and Figure S18 (Supporting Information)).

Under external loadings, the output voltage of the piezoionic elastomer steadily rises with increasing load resistance, while the output current gradually decreases (Figure 2e). When the external load resistance approaches the internal resistance of the piezoionic elastomer ($\approx\!6.2~k\Omega$), the elastomer achieves its maximum output power density, measuring at 1.3 $\mu W~cm^{-3}$ (Figure 2f). This value far exceeds that of conventional piezoelectric materials like ZnO (0.4 $\mu W~cm^{-3})^{[29]}$ and nylon-11 (0.6 $\mu W~cm^{-3})$, and piezoionic materials such as PVDF-HFP/LiTFSI ionogels (0.02 $\mu W~cm^{-3})$ and polyacrylamide (PAM) hydrogels (0.85 $\mu W~cm^{-3})$.

The voltage and current responses of the piezoionic elastomer vary with different thicknesses. Under the same pressure, thicker elastomers demonstrate lower transient voltage and current responses compared to thinner samples (Figures S19-S22, Supporting Information). This phenomenon is attributed to a broader distribution of local pressure as the thickness increases, leading to a reduction in pressure gradient.^[2] Moreover, the decay time of a thicker sample is longer than that of a thinner sample owing to the local pressure spreading over a larger area as the thickness increases.^[2] Under the constant pressure of 15 kPa, the decay time after the response could be as long as 5000 s for the pizoionic elastomer with a thickness of 1 mm (Figure 2g). Through time integration calculations, the maximum electrical energy is 1.26 µJ (Figure 2h). The energy conversion efficiency of the piezoionic elastomer is determined to be about 1.8% through integration of the force-displacement curve. This is comparable to previously reported conformal piezoelectric lead zirconate titanate nanoribbons (1.76%)[31] and biocrystal DLalanine thin film (1.08%),[32] and marking an order of magnitude

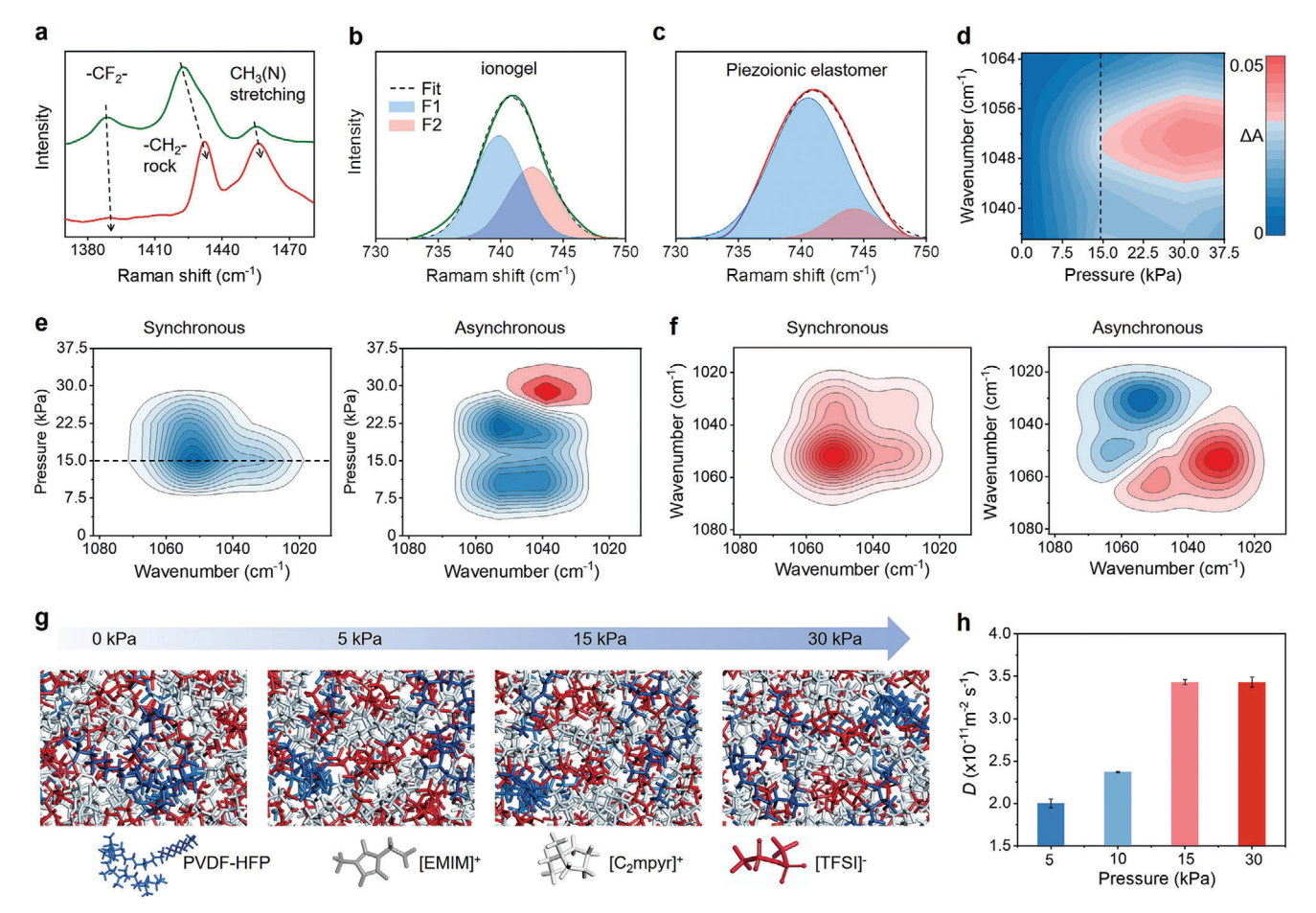


Figure 3. a) Raman spectra of the PVDF-HFP/EMIM TFSI ionogel (green line) and the piezoionic elastomer (red line) in the range between 1370 and 1500 cm⁻¹. b) Raman spectra of the PVDF-HFP/EMIM TFSI ionogel in the range between 730 and 750 cm⁻¹ and the corresponding fitting curves. c) Raman spectra of the piezoionic elastomer in the range between 730 and 750 cm⁻¹ and the corresponding fitting curves. d) The pressure-dependent FTIR spectra of the piezoionic elastomer under different pressures. ΔA is the absorbance difference at the peak of 1052 cm⁻¹ (—S—N—S— group) and calculated from the absorbance spectra in Figure S24 (Supporting Information). e) PCMW synchronous and asynchronous spectra generated from (d). f) 2D COS synchronous and asynchronous spectra generated from (d). In the PCMW and 2D COS spectra, the warm color (red) represents positive intensity, while the cold color (blue) represents negative one. g) The snapshots of the motion of [TFSI]⁻ anions under different pressures in the MD simulation model. h) Diffusion coefficients (*D*) of [TFSI]⁻ anions predicted by the MD simulation under different pressures.

enhancement compared to homogeneous and nanophase-separated piezoionic gels (about 0.3%, Figure S23 and Note S4, Supporting Information).

2.3. Ion-Interaction Mechanisms during Piezoionic Responses

To further investigate the response mechanism, molecular spectral analysis and molecular dynamic simulations are employed to uncover the ionic interactions during piezoionic transduction. Because infrared spectroscopy is effective in the analysis of polar groups, while Raman spectroscopy has advantages in analyzing nonpolar groups. The information provided by both infrared and Raman spectroscopies can complement and corroborate each other.[33–35] Upon introducing the IPC (C₂mpyr TFSI) into the PVDF-HFP/EMIM TFSI ionogel, wavenumber shifts are observed in the Raman spectra. The characteristic peak of the —CH₂— rock vibration in cations shifts from 1422 to 1431 cm⁻¹

(**Figure 3a**).^[36] The characteristic peak of the CH₃(N) stretching vibration of the imidazole ring in [EMIM]⁺ also shifts from 1455 to 1456 cm⁻¹, while the characteristic —CF₂— peak of PVDF-HFP shifts from 1388 to 1389 cm⁻¹.^[37,38] All of the shifts to higher wavenumbers indicate a robust cation—dipole interaction between cations and PVDF-HFP, confirming cation binding through the polymer network.^[10,36,39] Consequently, [TFSI]⁻ anions primarily act as the mobile ions for piezoionic responses. This also elucidates why pressing the positive electrode (working electrode) results in the generation of positive voltage, as it involves the movement of anions toward the negative electrode.

Besides, the chemical environment of the [TFSI]⁻ anions is also studied by Raman spectroscopy. The peaks at 740 cm⁻¹ (F1) and 745 cm⁻¹ (F2) represent the free [TFSI]⁻ anions and the bound [TFSI]⁻ anions, respectively.^[40] Upon adding IPC to the PVDF-HFP/EMIM TFSI ionogel, the peak area of F1 increases, indicating that the introduction of IPC weakens the confinement of [TFSI]⁻ anions and renders them more mobile (Figure 3b,c).

This can be attributed to the formation of an intermediate phase, which generates more free anions within the piezoionic elastomer. This dynamic process also serves as the foundation for the pressure-driven ion convection in the piezoionic elastomer. Attenuated total reflectance Fourier transform infrared (ATR-FTIR) spectroscopy in situ tracks the movement of [TFSI] anions in the piezoionic elastomer under different pressures (Figure 3d and Figure S24 (Supporting Information)). Because the cation–dipole interactions between cations and -CF2- in PVDF-HFP lead to the confinement of cations within the polymer network, the applied pressure mainly induces the movement of [TFSI]⁻ anions. The in situ ATR-FTIR spectra track the movement of anions at the pressurized terminal, with the characteristic absorption peak of -S-N-S- in [TFSI]⁻ anions at 1052 cm⁻¹.[10,37] As the pressure increases, [TFSI]- anions gradually move toward the unpressurized terminal, resulting in a decrease in the local concentration of [TFSI] anion at the pressurized terminal, manifested by a decrease in the intensity of the characteristic -S-N-S- peak in the ATR-FTIR spectra. When the pressure exceeds 15 kPa, the intensity of the characteristic peak at 1052 cm⁻¹ is almost unchanged, indicating that the movement capacity of [TFSI] anions reaches its maximum at the pressure of 15 kPa. This trend is in line with the results calculated from the perturbed correlation moving window (PCMW) spectra (Figure 3e and Note S5 (Supporting Information). At the pressure of 15 kPa, the absorption peak of [TFSI] anions undergoes the most significant change, indicating the maximum movement capacity of [TFSI]- anions at this point.

2D correlation spectroscopy (2D COS) provides additional insight into the behavior of [TFSI] anions during piezoionic transduction. With increasing force, the response sequence of the free [TFSI] anions at 1050 cm⁻¹ is prior to the bounded [TFSI] anions at 1063 cm⁻¹ (Figure 3f and Table S1 and Note S5 (Supporting Information)). This sequence correlates with the response times of voltage and current signals. The rapid increase in voltage is attributed to the quick response of free [TFSI] anions. Conversely, when pressure is continually applied to the piezoionic elastomer, the gradual increase and slow recovery of voltage/current signals are primarily attributed to the subsequent pressure-driven separation and movement of bound [TFSI] anions. Furthermore, classical field molecular dynamics (MD) simulations are performed to illustrate the motion of [TFSI] anions under different pressures. As pressure increases, the mobility of [TFSI]⁻ anions gradually escalates, reaching a plateau at ≈15 kPa (Figure 3g and Note S6 (Supporting Information)). The diffusion coefficient of [TFSI] $^-$ anions is predicted to increase from 2.0 \times $10^{-11} \text{ m}^{-2} \text{ s}^{-1}$ at 0 kPa to $3.32 \times 10^{-11} \text{ m}^{-2} \text{ s}^{-1}$ at 15 kPa, thus facilitating pressure-driven ion convection (Figure 3h).

2.4. Mechanical Properties and Comprehensive Comparison

The elastomer not only demonstrates outstanding electrical performance but also exhibits excellent mechanical adaptability. It can be easily bent and curled (Figure 4a). A piece of the elastomer with a thickness of 1 mm and width of 10 mm can lift a 1000 g weight without loosening or breaking, underscoring its high toughness (Figure 4b). Besides, it shows umbrella-like deformation but no rupture during puncture experiments with a sharp

needle, demonstrating excellent puncture resistance (Figure 4c). Time-temperature superposition curves reveal apparent activation energy (E_a) of 317 kJ mol⁻¹ for the physical cross-linking network in the piezoionic elastomer, comparable to the dissociation energy of typical C-C covalent bonds (350 kJ mol⁻¹, Figure 4d and Figure S25 (Supporting Information)).[41-44] This indicates a high energy contribution from cation-dipole interactions among polymer chains, providing the elastomer with high strength and toughness. In the piezoionic elastomer, [TFSI] anions interact effectively with the cations from both IL and IPC. The cation from IPC also forms the cation-dipole interaction with the polymer, ensuring the mechanical properties between the IPC and polymer. Although the introduction of IPC sacrifices some stretchability (maximum elongation at break of 508% compared to PVDF-HFP/IL ionogel's 610%), it brings a slight improvement in Young's modulus (0.36 vs 0.14 MPa) (Figure S26, Supporting Information).

Additionally, the reversible and dynamic cation-dipole interactions within the piezoionic elastomer facilitate self-healing.^[45] A fractured interface is rapidly healed under heating at 80 °C within 30 min (Figure 4e). The stress–strain curve further quantitatively evaluates the self-healing efficiency of the piezoionic elastomer after 30 min of healing (Figure 4f and Figure S27 (Supporting Information)). We comprehensively compare the Young's modulus, elongation at break, and fracture energy of the piezoionic elastomer before and after self-healing (Notes \$7 and \$8, Supporting Information). The self-healing efficiency range is 93-99%. Moreover, the piezoionic performance of the self-healed elastomer shows minimal degradation, still producing an opencircuit voltage of ≈90 mV and a short-circuit current of about 92 nA under 15 kPa pressure (Figure \$28, Supporting Information). To the best of our knowledge, this is the first demonstration of a piezoionic material achieving both self-healing properties and sensitive piezoionic voltages and currents. The molecular dynamics underlying the self-healing stem from the fast relaxation of cation-dipole interactions. [46] Analysis of rheological relaxation spectra reveals a fast relaxation at 0.6 s, indicating that the cation-dipole interactions between polymer chains can swiftly relax and reorganize, imparting the piezoionic elastomer with rapid self-healing capability (Figure 4g).

Owing to the fast relaxation of the cation-dipole interactions, the tensile curve of the piezoionic elastomer exhibits notable rate dependence. As the stretching rate increases, the Young's modulus rises (Figure 4h and Figure S29 (Supporting Information)). This occurs because overly rapid stretching rates, surpassing the relaxation time of the dynamic network, can lead to stiffening of the elastomer. At a strain rate of 0.33 s⁻¹, the toughness of the piezoionic elastomer reaches about 1400 J m⁻² (Figure S30 and Note S7, Supporting Information), [47] which is two orders of magnitude higher than that of piezoionic hydrogels (≈10 J m⁻²),^[48] and an order of magnitude higher than that of piezoionic ionogels ($\approx 100 \text{ J m}^{-2}$). [49] This value is even higher than that of natural cartilage ($\approx 1000 \text{ J m}^{-2}$). [48] Besides, even under a compression strain of 90%, the piezoionic elastomer maintains its structural integrity both before and after self-healing, without undergoing any fractures or breakage (Figure 4i). This underscores the exceptional pressure-resistant stability of the piezoionic elastomer.

Compared to previously reported piezoionic materials, our designed piezoionic elastomer addresses the longstanding

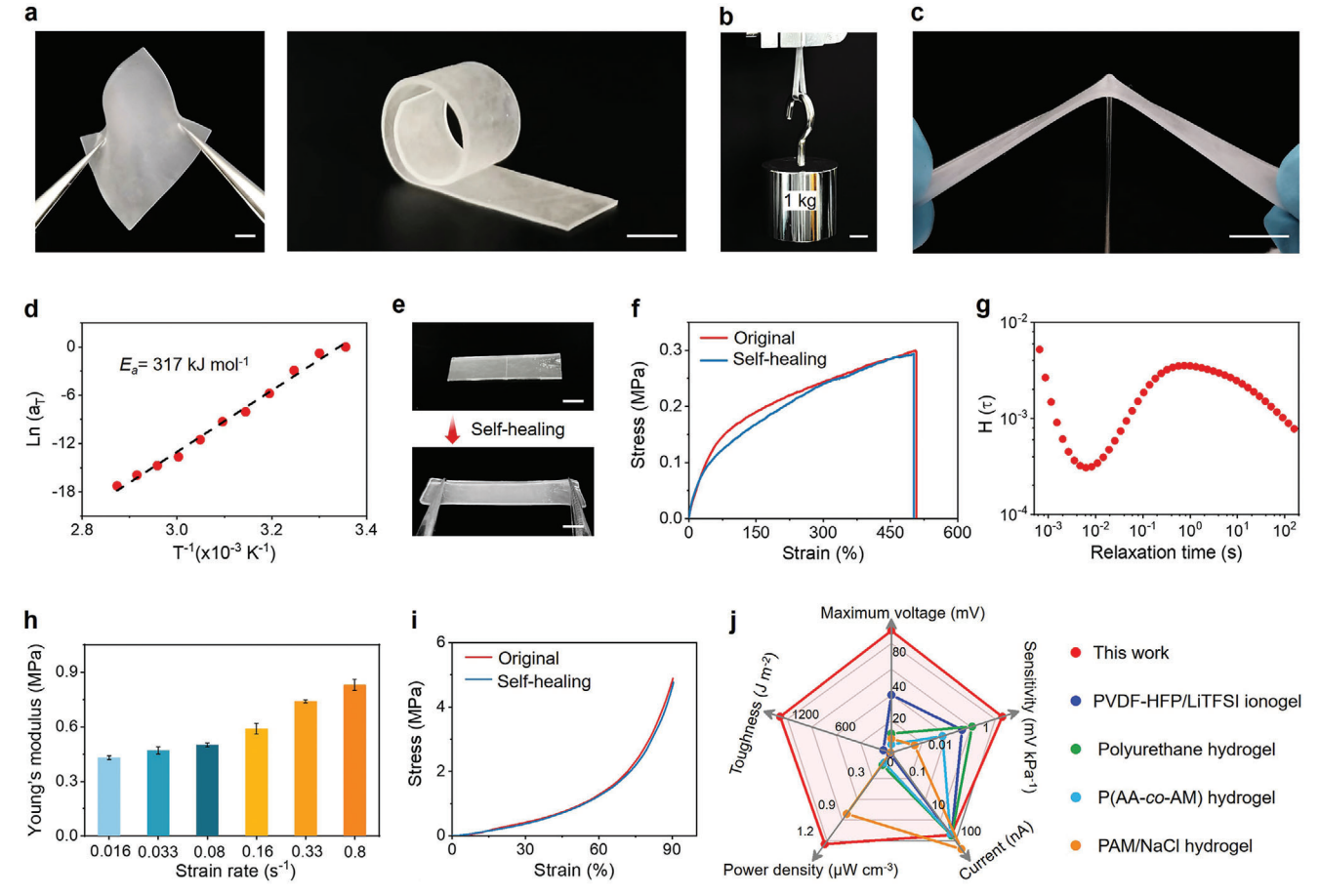


Figure 4. a) Photographs of the piezoionic elastomer during bending and curling. Scale bar: 10 mm. b) The piezoionic elastomer with a thickness of 1 mm and a width of 10 mm lifts a 1 kg weight. Scale bar: 10 mm. c) The puncture resistance of the piezoionic elastomer. Scale bar: 10 mm. d) The time–temperature horizontal shift factor (α_T) derived from the Arrhenius equation. e) Photographs of the piezoionic elastomer before and after self-healing at 80 °C for 30 min. Scale bar: 10 mm. f) The stress–strain curve of the piezoionic elastomer before and after self-healing. g) The rheological relaxation spectra of the piezoionic elastomer. h) Young's modulus of the piezoionic elastomer at different stretching rates. i) The 90% compression strain curve of the piezoionic elastomer before and after self-healing. j) The comparison of the piezoionic elastomer with previously reported piezoionic materials in terms of piezoionic coefficient, maximum voltage, current, power density, and toughness.

trade-off between electrical performance and mechanical properties (Figure 4j and Table S2 (Supporting Information)). By employing an intermediate phase and a dynamically cross-linked polymer network, the piezoionic elastomer achieves remarkable stretchability, high toughness, self-repair capability, and resistance to compression. This advancement overcomes the mechanical limitations of conventionally crystalline-based piezoelectric materials, ensuring their excellent mechanical adaptability in dynamic and stretchable ionotronic systems. On the other hand, compared to hydrogel- or organogel-based piezoionic materials, the toughness of the piezoionic elastomer is enhanced by at least an order of magnitude. The piezoionic elastomer also exhibits exceptional environmental stability, avoiding the evaporation of water or organic solvents and eliminating the need for complex encapsulation techniques. Furthermore, due to the stress concentration arising from microphase separation, the piezoionic coefficient (about 6.0 mV kPa⁻¹) is improved by a factor of 60 compared to previous piezoionic ionogels (about 0.1 mV kPa⁻¹).^[2] Meanwhile, the intermediate phase facilitates the generation of a substantial current through ion convection under pressure.

The combination of high voltage and large current results in an impressive output power density of 1.3 $\mu W~cm^{-3}$. This surpasses the performance of state-of-the-art piezoionic gels (e.g., about 0.85 $\mu W~cm^{-3}$ for PAM hydrogel, $^{[2]}$ about 0.17 $\mu W~cm^{-3}$ for polyurethane hydrogel, $^{[50]}$ and about 0.02 $\mu W~cm^{-3}$ for PVDF-HFP/LiTFSI ionogel $^{[2]}$).

2.5. Acoustic Perception, Pressure Mapping, and Logical Processing for Human-Machine Interaction

Due to the high sensitivity in piezoionic response, the piezoionic elastomer can perceive and identify spatial acoustic signals for human–machine interaction. When positioned 1 cm away from a loudspeaker (Figure 5a), it generates a real-time voltage of $70\,\mu V$ every time the A2 scale is played (Figure 5a). This demonstrates its ability to detect the acoustic vibrations. In a noisy environment, the piezoionic elastomer also produces different voltage responses to various environmental noises. When rain sounds are played, the elastomer produces a voltage change of $100\,\mu V$

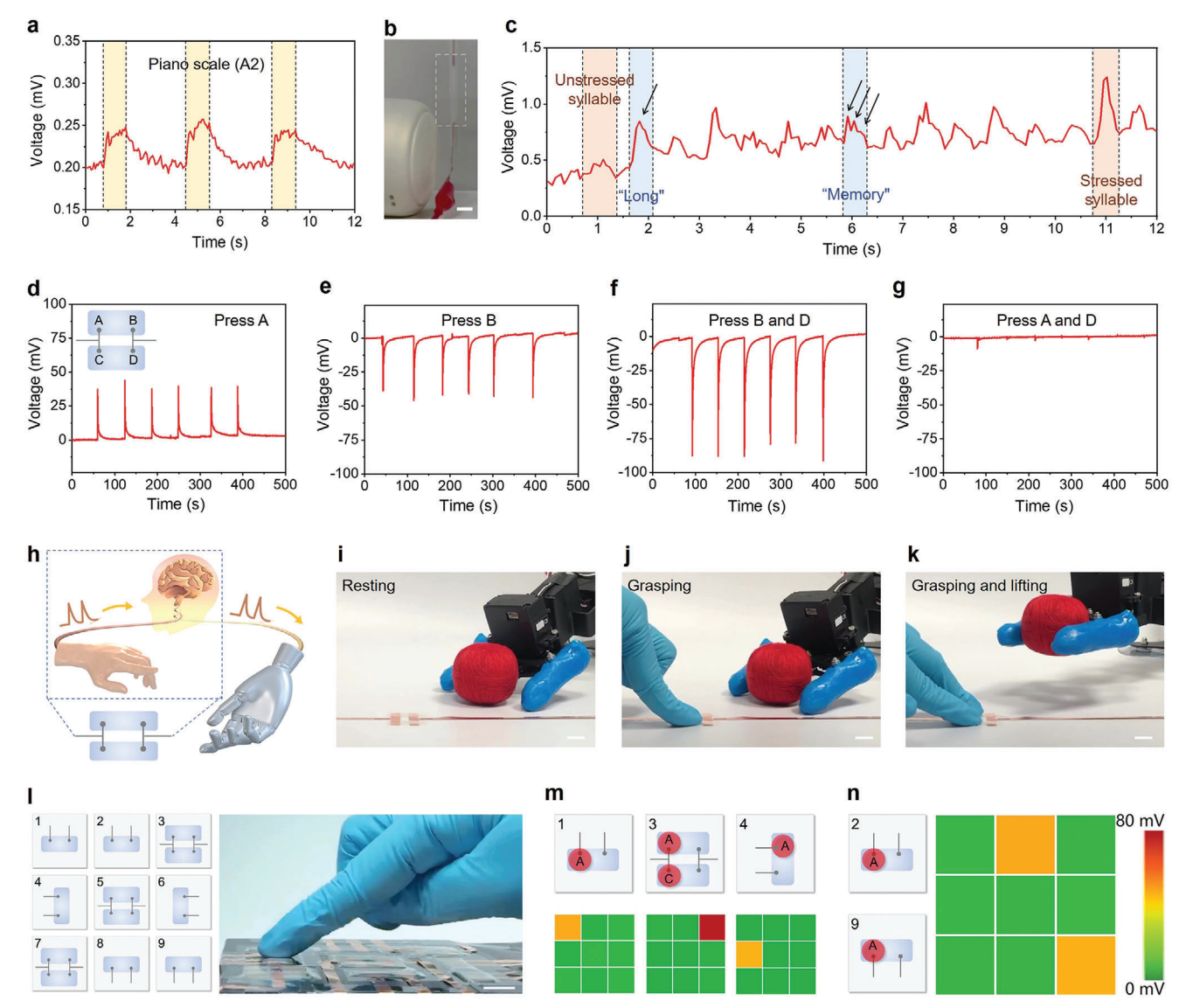


Figure 5. a) Voltage responses of the piezoionic elastomer each time the A2 scale is played. b) A photograph of the piezoionic elastomer positioned 1 cm away from a loudspeaker. Scale bar: 10 mm. c) Voltage responses of the piezoionic elastomer to human voices. d) Voltage responses when the terminal A is pressed. e) Voltage responses when terminals A and C are pressed simultaneously. f) Voltage responses when terminals B and D are pressed simultaneously. g) Voltage responses when terminals A and D are pressed simultaneously. h) Demonstration of the integration of two parallel piezoionic elastomers with a robotic arm. i) A photograph of the resting state of the robotic arm in the absence of pressure. Scale bar: 10 mm. j) A photograph of the robotic hand grasping a ball when terminal A is pressed. Scale bar: 10 mm. k) A photograph of the robotic arm grasping and lifting the ball when terminals A and C are pressed simultaneously. Scale bar: 10 mm. l) Schematic illustration of the piezoionic array sensing pressure and processing the input signal. Scale bar: 10 mm. m) Color change of the piezoionic array when different pixels are pressed. n) Color change of the piezoionic array when terminals A of pixels 2 and 9 are pressed simultaneously.

(Figure S31, Supporting Information). When thunder sounds are played, the voltage response of the elastomer reaches 200 μ V. This indicates that the piezoionic elastomer can discern changes in ambient noise through voltage responses. Moreover, the elastomer can perceive human talking through the piezoionic response. It exhibits varying voltage responses to stressed and unstressed syllables (Figure 5b and Movie S1 (Supporting Information)). An unstressed syllable produces a voltage change of about $10~\mu$ V, while a stressed syllable produces a voltage change of about $40~\mu$ V (Figure 5c). Furthermore, for a monosyllabic word like

"long," the voltage response waveform displays only one peak. By contrast, when the speaker enunciates a three-syllable word like "memory," the corresponding voltage response exhibits three peaks in the waveform. This underscores that the piezoionic elastomer can differentiate words in speech based on the magnitude of the piezoionic voltage and the peak number.

When pressure is applied to the elastomer, the dominant anion diffusion determines the direction and magnitude of the piezoionic response.^[2,51] In a single piece of piezoionic elastomer, the A (or C) terminal is connected to the positive

electrode (working electrode) of the nanovoltmeter, while the B (or D) terminal is connected to the negative electrode (reference electrode). This ionotronic system results in an anionically driven voltage response of ≈+40 mV when terminal A is pressed (Figure S32a, Supporting Information). Conversely, pressing the B terminal induces a voltage response of about -40 mV due to anion movement toward the positive electrode (Figure \$32b, Supporting Information). Simultaneously pressing both terminals A and B leads to nearly no voltage response (Figure S32c and Note S9, Supporting Information). This occurs because when A and B are pressed simultaneously, anion exchange takes place between the positive and negative terminals without forming a concentration gradient, thereby generating no voltage. Hence, when two pieces of piezoionic elastomer are connected in parallel and pressed at different spatial positions, the voltage responses vary accordingly (Movie S2, Supporting Information). Pressing terminal A in the parallel configuration generates a single voltage response of +40 mV (Figure 5d). Pressing terminal B results in an opposite response of -40 mV, which is similar to the voltage response of pressing a single piece of piezoionic elastomer, indicating that the piezoionic elastomer connected in parallel has almost no effect on the voltage response (Figure 5e). Similarly, simultaneous pressing terminals B and D produces a superposition of reverse voltage (-80 mV, Figure 5f), which is twice the voltage signal generated under a single press. Furthermore, when pressing terminals A and D simultaneously, the voltage signal essentially approaches zero (Figure 5g), further demonstrating the piezoionic elastomer's ability to perform logical addition and subtraction calculations after pressure perception.[52]

By harnessing the pressure sensing and signal processing capabilities, the piezoionic elastomer can engage in logical interactions between humans and robots. As a proof-of-concept demonstration, we integrated two parallel piezoionic elastomers with a robotic arm (Figure 5h). The threshold voltages for grasping the hand and lifting the arm are set to 30 and 60 mV, respectively. In the absence of pressure, the robotic arm remains at rest (Figure 5i). Pressing the A terminal produces a voltage response of ≈40 mV, which exceeds the grasping threshold and allows the robotic hand to securely grasp a red ball (Figure 5j and Movie S3 (Supporting Information)). Simultaneously pressing terminals A and C generates a voltage response of about 80 mV, which exceeds the arm lifting threshold. In this scenario, the robotic arm not only grasps but also lifts the red ball (Figure 5k and Movie S3 (Supporting Information)).

Furthermore, the piezoionic elastomer can be integrated into a tactile array, combining pressure mapping and logic processing capabilities. As an example, we construct a 3×3 array consisting of 9 pixels, in which pixels "3," "5," and "7" are constructed with two parallel elastomers while the other six are composed of single piezoionic elastomers (Figure 5l). The voltage range of the array is set from 0 to 80 mV, corresponding to a color shift from green to red. In the absence of pressure, the pixel array displays a green color. When terminal A of pixel 1 is pressed, it generates a voltage of about 40 mV, causing pixel 1 to transition rapidly to orange, with no observed signal crosstalk (Movie S3, Supporting Information). Simultaneously pressing terminals A and C of pixel 3 leads to a logical addition of the voltage signals, causing pixel 3 to turn red quickly. Subsequently, pressing terminal A of pixel 4 generates a voltage of about 40 mV, causing pixel 4 to turn

orange (Figure 5m). Besides, simultaneously pressing terminals A of pixels 2 and 9 results in two voltage responses of 40 mV each, with both pixels turning orange (Figure 5n).

3. Conclusion

In this study, we have implemented phase and interface engineering to effectively tackle the inherent trade-off between the electrical and mechanical properties of piezoionic and piezoelectric materials. This approach leverages the stress concentration in microphase-separated structures to generate high voltages, while ensuring rapid ion transport in both the soft and intermediate phases, leading to large currents. The elastomer showcases an exceptional piezoionic coefficient of about 6.0 mV kPa⁻¹ and an impressive power density of 1.3 µW cm⁻³ surpassing existing benchmarks in stretchable piezoionic materials. Its relatively high energy conversion efficiency (1.8%) holds promise for efficient power supplies in wearable ionotronics. Moreover, facilitated by the bridging effect of the intermediate phase engineering, the piezoionic elastomer demonstrates remarkable stretchability (the elongation at break of >500%), exceptional toughness (about 1400 J m⁻²), and rapid self-healing performance (within 30 min). Notably, when integrated into a circuit, this elastomer exhibits precise acoustic signal detection and highly sensitive spatiotemporal pressure signal processing. This study emphasizes the untapped potential of microphase-separated ionic elastomers with intermediate phases, offering a solution to the constraints of conventional piezoelectric and piezoionic materials, thereby advancing the field of energy-harvesting ionotronics and beyond.

4. Experimental Section

A detailed Experimental Section can be found in the Supporting Informa-

Supporting Information

Supporting Information is available from the Wiley Online Library or from the author.

Acknowledgements

The authors gratefully acknowledge the financial support from the National Natural Science Foundation of China (Grant No. 22305033 received by Z.L., Grant No. 52161135102 received by P.W.) and the Fundamental Research Funds for the Central Universities (Grant No. 23D210502 received by Z.L.).

Conflict of Interest

The authors declare no conflict of interest.

Data Availability Statement

The data that support the findings of this study are available from the corresponding author upon reasonable request.

Keywords

energy harvesting, human-machine interaction, ionotronics, piezoionic elastomers, soft materials

- [1] A. Chortos, Cell 2022, 185, 2653.
- [2] Y. Dobashi, D. Yao, Y. Petel, T. N. Nguyen, M. S. Sarwar, Y. Thabet, C. L. W. Ng, E. Scabeni Glitz, G. T. M. Nguyen, C. Plesse, F. Vidal, C. A. Michal, J. D. W. Madden, *Science* 2022, 376, 502.
- [3] W. Wu, Z. L. Wang, Nat. Rev. Mater. 2016, 1, 16031.
- [4] C. Yang, Z. Suo, Nat. Rev. Mater. 2018, 3, 125.
- [5] M. T. Chorsi, E. J. Curry, H. T. Chorsi, R. Das, J. Baroody, P. K. Purohit, H. Ilies, T. D. Nguyen, Adv. Mater. 2019, 31, 1802084.
- [6] Y.-M. You, W.-Q. Liao, D. Zhao, H.-Y. Ye, Y. Zhang, Q. Zhou, X. Niu, J. Wang, P.-F. Li, D.-W. Fu, Z. Wang, S. Gao, K. Yang, J.-M. Liu, J. Li, Y. Yan, R.-G. Xiong, Science 2017, 357, 306.
- [7] P. C. Sherrell, M. Fronzi, N. A. Shepelin, A. Corletto, D. A. Winkler, M. Ford, J. G. Shapter, A. V. Ellis, Chem. Soc. Rev. 2022, 51, 650.
- [8] F. Yang, J. Li, Y. Long, Z. Zhang, L. Wang, J. Sui, Y. Dong, Y. Wang, R. Taylor, D. Ni, W. Cai, P. Wang, T. Hacker, X. Wang, Science 2021, 373, 337.
- [9] K. Chen, D. Ho, Aggregate 2023, e425.
- [10] E. K. Boahen, B. Pan, H. Kweon, J. S. Kim, H. Choi, Z. Kong, D. J. Kim, J. Zhu, W. B. Ying, K. J. Lee, D. H. Kim, Nat. Commun. 2022, 13, 7699.
- [11] F. Li, X. Cai, G. Liu, H. Xu, W. Chen, Adv. Funct. Mater. 2023, 33, 2300701.
- [12] Z. Wang, T. Li, Y. Chen, J. Li, X. Ma, J. Yin, X. Jiang, Nat. Commun. 2022, 13, 6487.
- [13] Y. S. Zhang, A. Khademhosseini, Science 2017, 356, 500.
- [14] J. I. Lee, H. Choi, S. H. Kong, S. Park, D. Park, J. S. Kim, S. H. Kwon, J. Kim, S. H. Choi, S. G. Lee, D. H. Kim, M. S. Kang, Adv. Mater. 2021, 33, 2100321.
- [15] T. Someya, Z. Bao, G. G. Malliaras, Nature 2016, 540, 379.
- [16] S. Wang, Z. Sun, J. Bionic Eng. 2023, 20, 845.
- [17] Z. Lei, P. Wu, Nat. Commun. 2019, 10, 3429.
- [18] W. Li, L. Li, S. Zheng, Z. Liu, X. Zou, Z. Sun, J. Guo, F. Yan, Adv. Mater. 2022. 34, 2203049.
- [19] Z. Lei, P. Wu, Acc. Mater. Res. 2021, 2, 1203.
- [20] F. Nti, G. W. Greene, H. Zhu, P. C. Howlett, M. Forsyth, X. Wang, Mater. Adv. 2021, 2, 1683.
- [21] F. Makhlooghiazad, L. A. O'dell, L. Porcarelli, C. Forsyth, N. Quazi, M. Asadi, O. Hutt, D. Mecerreyes, M. Forsyth, J. M. Pringle, *Nat. Mater.* 2021, 21, 228.
- [22] D. L. Ma, Q. Q. Zhang, C. Z. Li, Angew. Chem., Int. Ed. 2022, 62, 202214931.
- [23] S. Tan, D. Zhang, E. Zhou, Polymer 1997, 38, 4571.
- [24] C. Zhang, W. Wang, P. Zhang, S. Yang, Polymer 2022, 256, 125196.

- [25] J. Kang, J. B.-H. Tok, Z. Bao, Nat. Electron. 2019, 2, 144.
- [26] T. Li, Y. Wang, S. Li, X. Liu, J. Sun, Adv. Mater. 2020, 32, 2002706.
- [27] K. G. Cho, S. An, D. H. Cho, J. H. Kim, J. Nam, M. Kim, K. H. Lee, Adv. Funct. Mater. 2021, 31, 2102386.
- [28] M. Wu, Y. Wang, S. Gao, R. Wang, C. Ma, Z. Tang, N. Bao, W. Wu, F. Fan, W. Wu, Nano Energy 2019, 56, 693.
- [29] T. Vijayakanth, S. Shankar, G. Finkelstein-Zuta, S. Rencus-Lazar, S. Gilead, E. Gazit, Chem. Soc. Rev. 2023, 52, 6191.
- [30] S. Anwar, M. Hassanpour Amiri, S. Jiang, M. M. Abolhasani, P. R. F. Rocha, K. Asadi, Adv. Funct. Mater. 2020, 31, 2004326.
- [31] C. Dagdeviren, B. D. Yang, Y. Su, P. L. Tran, P. Joe, E. Anderson, J. Xia, V. Doraiswamy, B. Dehdashti, X. Feng, B. Lu, R. Poston, Z. Khalpey, R. Ghaffari, Y. Huang, M. J. Slepian, J. A. Rogers, *Proc. Natl. Acad. Sci.* USA 2014, 111, 1927.
- [32] J. Li, C. Carlos, H. Zhou, J. Sui, Y. Wang, Z. Silva-Pedraza, F. Yang, Y. Dong, Z. Zhang, T. A. Hacker, B. Liu, Y. Mao, X. Wang, *Nat. Commun.* 2023, 14, 6562.
- [33] C. Chi, G. Liu, M. An, Y. Zhang, D. Song, X. Qi, C. Zhao, Z. Wang, Y. Du, Z. Lin, Y. Lu, H. Huang, Y. Li, C. Lin, W. Ma, B. Huang, X. Du, X. Zhang, Nat. Commun. 2023, 14, 306.
- [34] S. Liu, Y. Yang, H. Huang, J. Zheng, G. Liu, T. H. To, B. Huang, Sci. Adv. 2022, 8, eabj3019.
- [35] W. Qiu, C. Zhang, Q. Zhang, ACS Appl. Mater. Interfaces 2022, 14, 42578.
- [36] T. Chen, G. Ye, H. Wu, S. Qi, G. Ma, Y. Zhang, Y. Zhao, J. Zhu, X. Gu, N. Liu, Adv. Funct. Mater. 2022, 32, 2206424.
- [37] J. Kiefer, J. Fries, A. Leipertz, Appl. Spectrosc. 2007, 61, 1306.
- [38] C. E. Hathaway, J. R. Nielsen, J. Chem. Phys. 1964, 41, 2203.
- [39] Y. Cao, Y. J. Tan, S. Li, W. W. Lee, H. Guo, Y. Cai, C. Wang, B. C.-K. Tee, Nat. Electron. 2019, 2, 75.
- [40] Z. Cao, H. Liu, L. Jiang, Mater. Horiz. 2020, 7, 912.
- [41] H. J. Zhang, T. L. Sun, A. K. Zhang, Y. Ikura, T. Nakajima, T. Nonoyama, T. Kurokawa, O. Ito, H. Ishitobi, J. P. Gong, Adv. Mater. 2016, 28, 4884.
- [42] N. V. Lebedeva, A. Nese, F. C. Sun, K. Matyjaszewski, S. S. Sheiko, Proc. Natl. Acad. Sci. USA 2012, 109, 9276.
- [43] X. Li, J. P. Gong, Proc. Natl. Acad. Sci. USA 2022, 119, 2200678119.
- [44] M. Du, H. A. Houck, Q. Yin, Y. Xu, Y. Huang, Y. Lan, L. Yang, F. E. Du Prez, G. Chang, *Nat. Commun.* 2022, 13, 3231.
- [45] W. Zhao, Z. Lei, P. Wu, Adv. Sci. 2023, 10, 2300253.
- [46] Y. Wang, Y. Xie, X. Xie, D. Wu, H. Wu, X. Luo, Q. Wu, L. Zhao, J. Wu, Adv. Funct. Mater. 2023, 33, 2210224.
- [47] J. Wu, L. H. Cai, D. A. Weitz, Adv. Mater. 2017, 29, 1702616.
- [48] J.-Y. Sun, X. Zhao, W. R. K. Illeperuma, O. Chaudhuri, K. H. Oh, D. J. Mooney, J. J. Vlassak, Z. Suo, *Nature* 2012, 489, 133.
- [49] Y. Ding, J. Zhang, L. Chang, X. Zhang, H. Liu, L. Jiang, Adv. Mater. 2017. 29, 1704253.
- [50] M. S. Sarwar, Y. Dobashi, E. Glitz, M. Farajollahi, S. Mirabbasi, S. Nafic, G. M. Spinks, J. D. W. Madden, Proc. SPIE 9430, Electroactive Polymer Actuators and Devices (EAPAD), 2015, p.943026.
- [51] Z. Lei, P. Wu, Matter 2023, 6, 429.
- [52] H. Zhang, H. Zeng, A. Priimagi, O. Ikkala, Nat. Commun. 2019, 10, 3267.